

Design, operation and performance of the PAON4 prototype transit interferometer

R. Ansari¹, J.E Campagne^{1*}, D. Charlet¹, M. Moniez¹, C. Pailler¹, O. Perdereau¹, M. Taurigna¹, J.M. Martin², F. Rigaud², P. Colom³, Ph. Abbon⁴, Ch. Magneville⁴, J. Pezzani⁵, C. Viou⁵, S.A. Torchinsky⁶, Q. Huang^{8,1}, and J. Zhang^{7,1,8}

¹ LAL, Univ. Paris-Sud, CNRS/IN2P3, Université Paris-Saclay, 91405 Orsay, France

² GEPI, UMR 8111, Observatoire de Paris, 61 Av. de l’Observatoire, 75014 Paris, France

³ LESIA, UMR 8109, Observatoire de Paris, 5 place Jules Janssen, 92195 Meudon Cedex, France

⁴ CEA, DSM/IRFU, Centre d’Etudes de Saclay, 91191 Gif-sur-Yvette, France

⁵ Station de Radioastronomie de Nançay, Observatoire de Paris, PSL Research University, CNRS, Université d’Orléans, 18330 Nançay, France

⁶ APC, Université Paris Diderot, CNRS/IN2P3, CEA/Irfu, Observatoire de Paris, Sorbonne Paris Cité, 75205 Paris Cedex 13, France

⁷ College of Physics and Electronic Engineering, Shanxi University, Shanxi 030006, China

⁸ National Astronomical Observatories, Chinese Academy of Sciences, Beijing 100012, China

Accepted XXX. Received YYY; in original form ZZZ

ABSTRACT

PAON4 is an L-band (1250–1500 MHz) small interferometer operating in transit mode deployed at the Nançay observatory in France, designed as a prototype instrument for Intensity Mapping. It features four 5 meter diameter dishes in a compact triangular configuration, with a total geometric collecting area of $\sim 75\text{m}^2$, and equipped with dual polarisation receivers. A total of 36 visibilities are computed from the 8 independent RF signals by the software correlator over the full 250 MHz RF band. The array operates in transit mode, with the dishes pointed toward a fixed declination, while the sky drifts in front of the instrument. Sky maps for each frequency channel are then reconstructed by combining the time-dependent visibilities from the different baselines observed at different declinations. This paper presents an overview of the PAON4 instrument design and goals, as a prototype for dish arrays to map the Large Scale Structure in radio, using intensity mapping of the atomic hydrogen 21 cm line. We have operated PAON4 over several years and we have used data from observations in different periods to assess the array performances. We present preliminary analysis of a large fraction of this data and discuss crucial issues for this type of instrument, such as the calibration strategy, instrument response stability and noise behaviour.

Key words: Radio telescopes and instrumentation, Intensity Mapping, wide band interferometry, extragalactic H_I

1 INTRODUCTION

Despite the tremendous success of the Λ CDM cosmological model and the wealth of information provided by the analysis of CMB anisotropies (Hinshaw et al. 2013; Planck Collaboration et al. 2016, 2018), SNIa luminosities (Betoule et al. 2014) and optical surveys (see e.g. Salazar-Albornoz et al. 2017; Abbott et al. 2018; DES Collaboration et al. 2018),

the nature of Dark Matter and Dark Energy remain elusive (Bull et al. 2016) and a number of fundamental physics questions still need clarification. The Large Scale Structure (LSS) and its Baryon Acoustic Oscillation (BAO) feature are among the most powerful probes to constrain the cosmological model and Dark Energy and Modified gravity models (Amendola et al. 2013). The matter distribution at large scale in the universe is usually mapped through optical photometric and spectroscopic surveys.

The 21 cm line emission/absorption at 1.42 GHz due

* Email: campagne@lal.in2p3.fr

to the hyperfine transition of neutral atomic hydrogen (H_I) is a unique spectral feature in the L/UHF band which can be used to trace matter distribution from the vicinity of the Milky Way at very low redshifts, up to cosmological distances at $z \sim 1 - 3$, and into the Epoch of Reionisation (EoR) at redshifts well above 10. Using the 21 cm line to study the dark ages and the EoR has been considered for more than 20 years (see e.g. [Furlanetto et al. 2006](#); [Pritchard & Loeb 2008](#)) and several experiments have been carried out or ongoing to detect the 21 cm signal from the EoR. These include: LOFAR ([van Haarlem et al. 2013](#)), MWA ([Tingay et al. 2013](#)), PAPER ([Parsons et al. 2010](#)), HERA ([Pober et al. 2014](#)), NenuFAR ([Zarka et al. 2015](#)) ...

As noted already more than a decade ago ([Abdalla & Rawlings 2005](#); [Peterson et al. 2006](#)), mapping the 3D distribution of matter using H_I as a tracer is an elegant and complementary approach to optical surveys to constrain cosmological parameters and Dark Energy through the study of LSS and BAO. The early proposals were considering the observation of individual galaxies at $\lambda = 21$ cm, requiring very large collecting area and sensitivities, which is expected for SKA ¹ ([Braun et al. 2015](#)).

However, it was soon realised that the study of LSS with the 21 cm emission could be carried out through the Intensity Mapping technique, without the need to resolve individual H_I sources, and with less stringent requirements on instrument sensitivity. To perform such a survey, a wide band instrument with a wide field of view is required, operating in the L/UHF band, from a few hundred MHz to 1400 MHz ($\nu = 1420.4/(1+z)$ MHz), while a modest angular resolution of a fraction of a degree ($\sim 10'$) would be enough to determine the matter power spectrum on the scales most useful for Cosmology ([Chang et al. 2008](#); [Ansari et al. 2008](#); [Wyithe et al. 2008](#); [Peterson et al. 2009](#)).

This approach has a major drawback even without considering the instrument noise and Radio Frequency Interference (RFI). Indeed, the component separation is much more difficult than for the CMB extraction, as foreground emissions dominated by the Milky Way synchrotron emission and the radio-sources has a brightness temperature ~ 10 K, so a few thousand times brighter than the cosmological signal which is of the order or below 1 mK. The smooth frequency dependence of the synchrotron emission is the key to solving this daunting task. The problem is similar for experiments looking for the 21 cm signal from the EoR and has been studied by a number of authors (e.g. [Wang et al. 2006](#)).

The detectability of the cosmological 21 cm signal at lower redshifts ($z \lesssim 3$) in the presence of foregrounds has been subsequently studied (e.g. [Ansari et al. 2012b](#); [Wolz et al. 2014](#)). The advantages of the m-mode analysis for map making and foreground subtraction, applicable for a transit type interferometer is discussed in [Shaw et al. \(2014\)](#) and extended to the polarisation case in [Shaw et al. \(2015\)](#).

The interest in Intensity Mapping (IM) as a tool for cosmological and Dark Energy surveys has grown over the last decade, with broadened science reach ([Bull et al. 2015b](#); [Cosmic Visions 21 cm Collaboration et al. 2018](#)). A number of groups have engaged in exploiting existing instruments to carry Intensity Mapping surveys, for example using GBT

([Chang et al. 2010](#); [Masui et al. 2013](#)) or plan to do so with SKA and its pathfinders ([Bull et al. 2015a](#)), or with single-dish telescopes ([Bigot-Sazy et al. 2015](#)) such as FAST ([Bigot-Sazy et al. 2016](#)).

Other groups are building specifically designed instruments for such surveys. Most groups plan to use dense interferometric arrays, associated with high throughput digital beam-forming and digital correlators that can fulfil the instrumental requirements for IM surveys. Single dish instruments combined with multi-feed receivers provide an alternative instrumental design. A 7-beam receiver covering the frequency band 700 – 900 MHz has been considered for the GBT ([Chang & GBT-HIM Team 2016](#)) and a ~ 50 feed receiver will be built and placed at the focal plane of an off-axis reflector by the BINGO team ([Battye et al. 2013](#); [Wuensche & the BINGO Collaboration 2018](#)).

Dedicated IM instruments share a number of common features and problems with wide field arrays built or under development to search for the EoR signal (LOFAR, MWA, PAPER, HERA, NenuFAR ...), although the latter observe at much lower frequencies ($\nu \sim 100$ MHz, $z \sim 10$). Two main options are considered for IM interferometric arrays. Either cylindrical reflectors, oriented north-south, possibly with FFT beam-forming along the cylinder axis, or an array of dishes, with pointing capability in declination. FFT beam-forming is also possible using a regular grid of antenna, including dishes, as mentioned by ([Tegmark & Zaldarriaga 2009](#)). Such a strategy has already been implemented on a modest scale in individual LOFAR stations for the High Band Array, and at ~ 1 GHz frequencies in EMBRACE ([Torchinsky et al. 2016](#)). This was the ultimate goal of the SKA mid frequency array with an early demonstrator called 2-PAD ([Armstrong et al. 2009](#)).

CHIME ([Bandura et al. 2014](#)), which is among the most advanced IM projects, uses an array of cylinders, as pioneered by the Pittsburgh Cylindrical Telescope (PCT) prototype ([Bandura 2011](#)). The HIRAX project ([Newburgh et al. 2016](#)) plans to build a large array of 6 meter dishes, in South Africa, close to the SKA site, and larger arrays, such as the proposed PUMA are being considered ([Bandura et al. 2019](#)).

Development of the PAON4 array and the data analysis procedures has been closely linked with the Tianlai project effort. Tianlai is an NAOC-led project ([Das et al. 2018](#); [Chen 2012](#)) which is currently operating two pathfinder instruments in a radio quiet site in the Xinjiang province of western China. The first Tianlai instrument is composed of three cylinders, each 40m long and 15m wide, equipped with a total of 96 dual polarisation receivers. The Tianlai instrument concept was extended by including a second array (Tianlai16D) composed of 16 steerable, 6 meter diameter dishes, in a dense circular configuration, after initial evaluation and design work for PAON4. We have carried out studies to optimize the PAON4 and Tianlai16D array configurations and evaluate their performances ([Zhang et al. 2016a,b](#)).

This paper is organised as follows. The PAON4 instrument design and project history is presented in Section 2. Section 3 presents an overview of the electronics chain, the software correlator and the acquisition system. The instrument operation and the survey are described in Section 4, while the data analysis pipeline is discussed in Section 5. Section 6 presents the instrument performance and some pre-

¹ SKA organisation: <https://www.skatelescope.org/>

liminary results from the ongoing survey. The paper goes on with an outline of our future plans for PAON4, before coming to some concluding remarks.

2 PAON4 INSTRUMENT DESCRIPTION

Preliminary design of a small dish interferometer at Nançay began in 2010. The project, subsequently named **PA**raboles à l'**O**bservatoire de Nançay (PAON - Paraboloïdes at the Nançay Observatory), was approved in spring 2012 by the partner institutes: LAL-CNRS/IN2P3, Observatoire de Paris, and Irfu/SPP (CEA). The goal is to evaluate specific issues of dense interferometric arrays operating in transit mode. In particular, the project investigates:

- Electromagnetic coupling between neighbouring receivers at close distance and the impact on the correlated noise
- Array stability and the gain and phase calibration using bright sky sources
- Data analysis and sky map reconstruction from time dependent visibilities

During a short test period from autumn 2012 to summer 2013 two 3 m diameter dishes were used for observation at Nançay. Meanwhile, the PAON4 reflectors were designed and manufactured. The mount and reflectors were assembled on site during end of spring/summer 2014 and then equipped with the receivers and electronic modules in autumn 2014. First observations were carried out in winter 2015, and the instrument was formally inaugurated in April 2015. The four reflectors are visible in the photograph shown in Fig. 1, taken from a point south-west of the array.

2.1 Array configuration

The PAON4 interferometer is composed of four 5 m diameter parabolic $F/D=0.4$ reflectors and has a combined collecting area of $\sim 75\text{m}^2$ ($\sim 65\text{m}^2$ effective area). It is hosted at the Nançay radio observatory², in France, about 200 km south of Paris. The array (central antenna) is located at latitude $47^\circ 22' 55.1''$ N, and $2^\circ 11' 58.7''$ E longitude.

The PAON4 compact triangular configuration was selected after comparison of several possibilities. The chosen configuration provides 6 independent baselines, which is the maximum possible with 4 antennas, compared to 4 baselines for a rectangular 2×2 configuration (Zhang et al. 2016b). Three dishes are positioned at the three vertices of an equilateral triangle with 12 m sides, while the fourth dish is located close to the center of triangle. In addition to the four auto-correlations signals (zero length baseline), there are six independent baselines, as shown in the array layout schematic of Fig. 2. One baseline (1-2) is aligned with the East-West direction, one baseline (3-4) lies along the North-South direction, and the four other baselines have both EW and NS components.

The receiver on each reflector is made of a cylindrical

feed with two probes sensitive to two polarisations. The H-probe is sensitive to the electric field parallel to the EW direction, and the V-probe is sensitive to the field in the meridian plane. There are thus a total of 8 RF signals from the four feeds: four H-polarisation signals and four V-polarisation. These are amplified, filtered, and frequency shifted to VHF band before being digitised. The digitised signals are processed in real-time by a small cluster of acquisition computers which calculate all correlations. Two additional RF signals passing through identical analogue and digital electronic chains before being fed to the acquisition computer were subsequently added. The first one, called RFIMON, carries an RF signal from a simple dipole antenna and is used to monitor the RFI environment in the PAON4 band. The second RF signal comes from a $50\ \Omega$ resistor connected to the input of a LNA, identical to the one which equips the H and V probes. This RF signal, referred to as THERMON, is used to monitor the temperature dependent gain variations of the analogue electronic chain and correct for it. This is discussed further in Section 5. PAON4 also includes a standard temperature probe which is read every few minutes, providing temperature variations of the antenna environment. The mount, reflector and feed design is discussed hereafter, and the electronic chain and the software correlator are described in Section 3

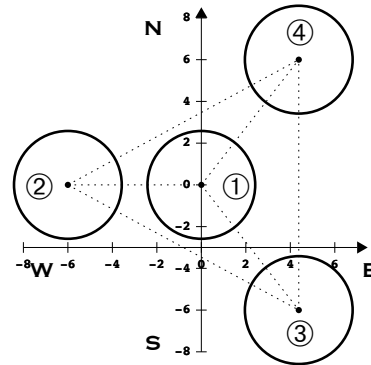


Figure 2. PAON4 array layout (coordinates are in meters).

2.2 Reflectors and feed design

The antennas were designed and built at the Observatoire de Paris GEPI laboratory and by industry subcontractors. The design has been chosen in order to fulfil the following requirements:

- build four prototype antennas with 5 m diameter with a parabolic reflector;
- build a robust antenna architecture to be able to sustain historical storm conditions in the region of Nançay (i.e. speed wind of about 130 km/h) as well as snow and ice during severe winter conditions;
- permit the dish motorization to orient them in a broad range of elevation (declination) angle;
- limit as far as possible the cost while ensuring reliable operations for 10 years or more.

Some design parameters are summarized in Table 1 and the whole array is shown in Fig. 1.

² Nançay radio observatory, <https://www.obs-nancay.fr/>



Figure 1. PAON4 dish array interferometer at Nançay, viewed from the south-west.

The mechanical structures of the antennas are standard steel structure elements which underwent anti-corrosion treatment by hot-dip galvanizing, and were prepared (cut, drilled) by numerically controlled machines by the subcontractor. Each parabola is made of 12 petals for logistic reasons. Each petal is made of a laser-cut stainless steel sheet with a carefully hand-installed reflector mesh. About 600 hours were required to install the mesh at the GEPI laboratory. The surface deviations of the mesh were kept as low as possible, and they were measured after the mounting at a level of $\lambda/70$ r.m.s.. This design is well adapted for a project on the scale of PAON4, but for a larger array a more automated process would be required since non-negligible manpower on site was required for the mounting of the 48 petals.

Asynchronous motors with reduction gears and non-reversible trapezoidal screws are used for the declination axis pointing. The rotation of the motor is selected by embedded software, and takes into account the stop phase duration for better pointing precision. The position of the parabola is controlled by an accelerometer which is installed in a sealed control command box and is therefore fully protected against the weather conditions, unlike the position encoders. In addition to performing pointing measurements, the accelerometer can monitor any small angular displacement of the antennas such as those due to possible ground instabilities. A running mean of 2000 samples is performed in order to measure the position of each parabola. The pointing of the antennas is controlled by scripts or by an embedded web server accessible through the internet. A precision of $\sim 0.1^\circ$ has been measured on site.

The PAON4 antennas are installed near the EMBRACE prototype (Torchinsky et al. 2016), and could therefore be easily connected to the electric mains and Ethernet network. At this place, the ground is particularly loose and in order to avoid having to build expensive and fixed concrete foundations, the antenna structures are slightly flexible with respect to horizontal stability, and are equipped with four legs

Table 1. Main design parameters of PAON4 dish and feed.

Dish	
Diameter reflector	5 m
f/D	0.4
L x W x H	6 m x 5 m x 5.4 m
roughness(design)	$\lambda/50$ at 21 cm
zenith angle	15°N to 38°S
Total weight	2.2 t
Feed & choke & probes	
Diameter “choke”	360 mm
Height “choke”	80 mm
Distance from entrance	10 mm
Thickness	1.5 mm
Diam. internal “feed”	158 mm
$\Delta D/D$	$5 \cdot 10^{-3}$ (0.8 mm)
Thickness	4.5 mm
Height (total)	377 mm
Probes	2 (linear)
Probe (Diam./Length)	6.2 mm/50.2 mm
Conic part of the probe	2.5 mm
Distance probe-end cap	79.2 mm
Base	N std. Radiall R 161 404
Gain (meas./simu)	9.5 dB/10.34 dB

in a statically undetermined configuration. In addition, the rotation axis bearings include kneecaps.

The feed design was adapted to the dish diameter, taking into account the needs of two orthogonal linear polarisations and the total bandwidth [1250, 1500] MHz. It uses a classical circular wave guide with a choke. The geometric parameters are listed in Table 1 and shown in the sketch of Figure 3 (left panel). The guide has a diameter of 158 mm and a length of 377 mm machined inside a aluminium guide 4.5 mm thick. The cut-off frequencies are 1110 MHz for

the TE11 mode and 1460 MHz for the TM01 mode making the feed system single moded throughout the bandwidth except in the upper 40 MHz. The guide wavelength is $\lambda = 543, 341, 299$ mm at 1250, 1420, 1500 MHz. The machining guarantees a circular tolerance of $\Delta D/D = 5 \times 10^{-3}$ (0.8 mm) for a cross-polarization isolation of -30 dB. This feed is suitable for the PAON4 bandwidth but could not be easily adapted to a larger bandwidth. The probes are made with brass rods of relatively large diameter to have the possibility of larger bandwidth in the future. The conic shape of the rod minimizes the impedance mismatch with the base. The exact locations of the probes inside the circular guide have been optimized by simulation and verified by measurement *a posteriori*. The choke design has also been optimized by simulation to reduce side lobes as much as possible.

Figure 3 (right panel) shows the manufactured feed. The feed is maintained at the focal location by three fibreglass hollow bars to optimize the electromagnetic transparency of the supports while ensuring robustness during high wind conditions. The radiation diagram of the feed alone has been simulated and then measured with good agreement, as shown on Figure 4.

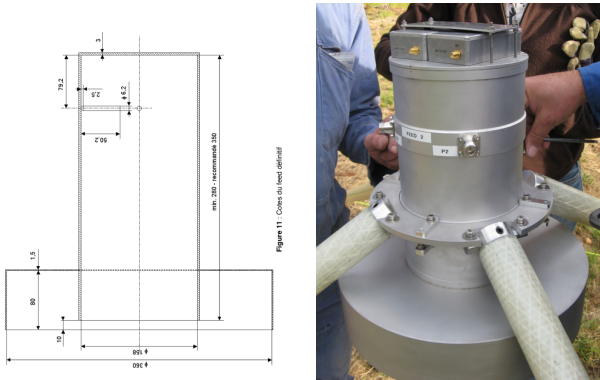


Figure 3. PAON4 feeds: left schematic drawing with feed dimensions. Right: photograph of a feed; the two amplifiers for H and V probes are located in the two boxes at the top.

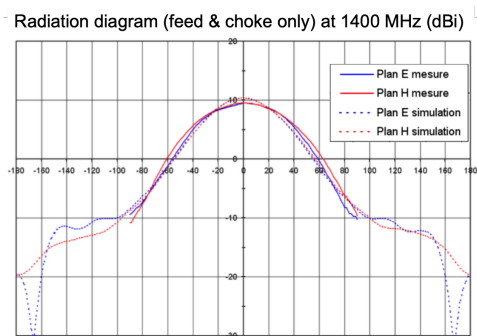


Figure 4. Radiation diagram of the feed and choke: measurement (solid lines) and simulation (dashed lines).

3 ELECTRONIC AND ACQUISITION SYSTEM

PAON4 has been equipped with the analogue and digital electronic modules developed in the BAORadio project,

started in 2007, mostly as digital components for a 21 cm H_I Intensity Mapping survey (Ansari et al. 2012a). The ADC boards being used in PAON4 were one of the main components of this system, each being capable of digitising 4 RF signal at 500 MHz sampling rate, and performing on-the-fly FFT within their FPGA, with 61 kHz frequency resolution (Charlet et al. 2011).

An analogue RF amplification, filtering, local oscillator and mixer had also been designed and realised for testing the digital components boards with the PCT (Pittsburgh Cylindrical Reflectors). Only the LNA have been specifically designed and made for PAON4. It must be clear that the electronic chain, and more specifically the analogue components have been designed for testing purposes and should not be considered as state of the art.

The BAORadio electronic and data acquisition software has been used several times on the PCT at Pittsburgh (Bandura 2011), processing the signals from up to 32 feeds in 2010, computing the full set of 512 correlations, over a reduced band of ~ 50 MHz. It has also been used on the FAN project (Deschamps et al. 2013) and successfully deployed at the NRT (Nançay Large Radio Telescope) for the HICluster program, searching for H_I in nearby clusters (Ansari et al. 2016).

3.1 Analogue and digital electronic

An overall schematic view of the PAON4 analogue electronic chain is shown in Fig. 5. On the feed, the amplifier circuit consists of two LNA's interconnected through a low pass filter. It is connected to the probes through 10 cm cables. An Avago/Broadcom MGA633 GaAs MMIC ultra low noise amplifier is followed by a Qorvo SPF5122 LNA, and a low pass filter is inserted between the two LNAs to lower the power at the input of the second one. The total gain is 30 dB and the noise factor $NF \sim 0.6$ dB, leading to a noise temperature of $T_a \sim 50$ K for the first stage amplifier ($F = 1 + \frac{T_a}{290K}$; $NF = 10 \log_{10}(F)$). An 8 meter RG142 cable connects the feed amplifiers to the second stage amplifier on the antenna. This stage consists of two SPF5122 LNA and provides an additional gain of 30 dB, which is connected to the frequency shifter in the main analogue electronic cabinet on the central antenna with a second 8 meter RG142 cable. After an RF filter, the signal is amplified before the down conversion is performed. An ADF4360 – 5 PLL and VCO frequency synthesizer delivers a 1250 MHz signal to a JMS – 11X frequency mixer. The signal is down converted in the $[0 - 250\text{MHz}]$ VHF band. Additional VHF amplification is performed and a low pass filter (20 dB at 1500 MHz) eliminates the high frequencies part of the signal. The RF card output is connected to the ADC board in the EMBRACE (Torchinsky et al. 2016) container by two 50 Ω RG58 cables. A first 40 meter cable brings the signal to the feedthrough panel at the container wall, followed by a 10 meter cable from the feedthrough panel to the PAON4 digital electronics.

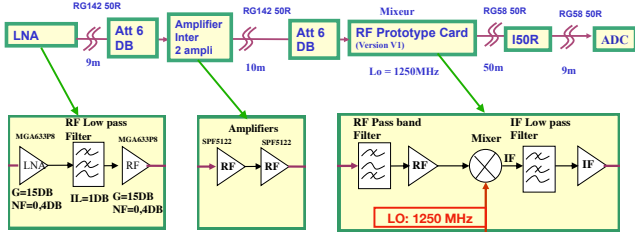


Figure 5. Schematic view of the PAON4 analogue electronic chain

Each BAORadio ADC board include two (ADC+FPGA) blocks sharing a common control electronic. Each block handles two analogue inputs which are sampled at 500 Msample/s with 8 bits dynamic range. Each block transmits data through high speed optical links to dedicated PCIExpress reception boards in the acquisition computers. The eight PAON4 RF signals (4 H-pol + 4 V-pol) are thus digitised by two ADC boards, and data transmitted to the acquisition computers located few hundred meters away, through 4 optical fibres. A third ADC board handles the RFIMON and THERMON channels, which are treated separately by the acquisition computer, without going through the correlator. The ADC boards receive a common master clock and trigger signals, and the board configuration and control through USB links. Two different firmwares can be loaded on the ADC board FPGA's. The first one, called the RAW firmware is used to digitise signal and transmit waveforms to the acquisition computers. The RAW firmware can handle a maximum of 48k samples corresponding to 96 μ s long digitisation frames. The second firmware, called the FFT firmware performs waveform sampling, Fourier transform (FFT), clipping and then transmits the Fourier coefficients (2 bytes complex numbers) for 8k samples digitisation frames corresponding to 16 μ s in time and 4096 Fourier coefficients with 61 kHz frequency resolution. Each digitisation frame is time-tagged with the 125 MHz FPGA clocks and the digitisation frames on different FPGA's are synchronised by the external trigger signal. The BAORadio ADC boards can cope with a maximum trigger rate of ~ 30 kHz, corresponding to $\sim 50\%$ live time on the sky. However, the current acquisition computer system and software correlator can only cope with a trigger rate of $\lesssim 5$ kHz, corresponding to $\lesssim 10\%$ live time. We have carried observations with the FFT firmware till the end of early 2016, but results discussed in this paper are mostly based on data taken with the RAW firmware. The digital data stream, either waveform or Fourier components are transferred over optical fibres to the software correlator-acquisition computer cluster located 300 meters away, in the Nançay computer building.

3.2 Data acquisition and software correlator

The data acquisition system is composed of a cluster of computers located in dedicated room in Nançay interconnected through a private 10 Gbit/s Ethernet network in addition of the external 1 Gbit/s Ethernet network. An additional computer connected through this Nançay network is located in the EMBRACE container, and handles the control of the

ADC boards through USB communication with the 4 antennae pointing controllers through another dedicated network, as well as various network controlled equipments, such as power supplies, local oscillator (LO) control, as well as the thermometer readout. The acquisition/software correlator system itself is composed of six (6) computing nodes and an additional machine, which acts as the acquisition controller and supervisor. The computing nodes are arranged in two layers: 4 of them form the first layer (front-end machines) which receive data from the two ADC boards, through four optical links. The two nodes forming the second layer perform the correlation computations. Figure 6 shows a schematic view of the system configuration. The acquisition and processing of the two ancillary RFIMON and THERMON signals is done by an independent computer, running the same software.

The front-end machines perform FFT on the received data streams, except when the FFT firmware is used, then divide the frequency bands into a number of sub-bands corresponding to the number of computing nodes in the correlator layer. Each front-end machine receives the data corresponding to two RF signals, currently arranged as a pair of same polarisation, H-H or V-V signals. Fourier components for each sub-band is send to the corresponding compute node in the correlator layer, which has currently two nodes, each computing 36 correlations or visibilities for 2048 frequency channels, over 125 MHz band, half of the full ADC board Nyquist sampling limit of 250 MHz. The 36 computed visibilities correspond to the following pairs:

- 8 auto-correlations, 4 corresponding to the H signals, and 4 to the V signals
- 12 visibilities corresponding to the cross correlations between the same polarisation signals. There are 6 H-H and 6 V-V cross-correlations between H-polar and V-polar signals from the 4 feeds
- Sixteen visibilities corresponding to H-V cross-correlations between H-polarisation signal from one feed and V-polarisation signal from the second feed

The total data rate ingested by the front-end machines at $\sim 10\%$ live time on sky corresponds to ~ 400 MB/s, with a factor 4 higher rate exchanged between the two layers, as the FFT computation is carried with 4-byte floating point numbers. The visibility time sampling is also a parameter, although we have used typical sampling rate of one or a few seconds. Most data discussed here has been taken with a visibility sampling rate of 3 or 6 seconds. Computed visibilities are saved into permanent storage (disk) every few seconds, and a number of visibility matrices, defined again by input parameters are grouped into a single file. We have used ~ 100 MB files, and 24 hours of data represent a total of 70 GB at 3 second sampling rate.

The data acquisition and correlator software, **TAcq**, has also been developed in the framework of the BAORadio project, starting from 2007 and has been enhanced over the years. It is a flexible, high performance C++ software package, which uses the SOPHYA³ class library for standard numerical algorithms and I/O. Thanks to its flexibility and various operation modes, TAcq can be used at different

³ SOPHYA C++ class library : <http://www.sophya.org/>

stages of the project, from final tests of the electronic system boards, to the routine operation of the interferometer, as well as during commissioning.

The TAcq package defines a simple and very efficient multi-threaded architecture, where different threads cooperate through a central memory manager hub. The number of running threads is also dynamically determined through the parameters, which should be tuned to a given hardware configuration. A description of the software architecture, the different classes and system operation modes are beyond the scope of this paper and will be discussed in a separate, forthcoming publication.

In practice, a main program called **mfacq** with different operation modes, controlled by an extended set of parameters handles the acquisition and correlation computation tasks. The control node spawns one mfacq process on each of the compute nodes, the four front-end nodes and the two nodes in the correlator layer for PAON4, and provides each process their specific set of parameters. The complete system operates in streaming mode, with data packets exchanged between mfacq processes through the network layer. The time synchronisation for visibility computation is insured thanks to the hardware time tags which are propagated through the data packet streaming protocol.

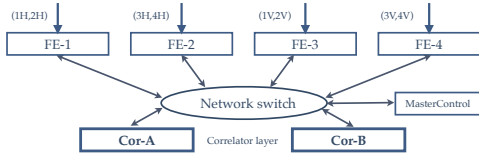


Figure 6. Schematic view of the PAON4 acquisition and correlator system

4 OPERATIONS AND OBSERVATIONS

After the completion of its construction (mid 2015), the PAON4 observations served several aims in successive periods, with few minor hardware or software changes. Observations carried out in 2015 were mostly dedicated to hardware debugging, from finding faulty cables and electronic modules to identifying some RFI sources. For example, an Ethernet switch was initially installed in the central antenna electronic cabinet, to ensure the readout of a temperature sensor, and was generating RFI. We also spend some time measuring correlated noise, both on the instrument and in the lab, in 2015 and 2016. Correlated noise measurement in the lab showed that its main source was couplings through the power supply. The overall system was subsequently improved, by better shielding, more careful ground wiring and an improved power supply system. The correlated noise level was reduced by a factor 10 in this process. Gain variations and some randomly occurring perturbations were observed. Clarifying their sources and curing or correcting these effects consumed significant time and effort, in 2017 and early 2018, as discussed in section 5.

One of the PAON4 signals, the 4V channel was blinded in May 2016, by connecting its front-end LNA to a 50 Ω

resistor, as a tool for understanding the source of perturbations (see section 5.1) and gain variations (see 5.2). The 4V channel was unblinded and the additional THERMON signal was added to the system in July 2018, after the identification of the perturbation source. In 2015 and 2016, we were operating PAON4 with the FFT firmware loaded on the ADC boards. The ADC boards were then sending FFT coefficients to the software correlator. We switched to the RAW firmware in February 2017, in order to investigate some problems with the FFT firmware, including possible saturation by positioning satellite signals due to limited dynamic range of the FFT firmware. We also added two front-end nodes to handle FFT computation by the acquisition/correlator software.

Data taking is automatic once all acquisition parameters are set, and can be remotely initiated and monitored. After each acquisition run, data are transferred to the IN2P3 computing center for analysis and archival. An SSH connection to the acquisition cluster is currently necessary for launching the data taking. It is used to point the antenna and configure the digitisation boards, and the check or modify the acquisition parameters such as the visibility sampling rate the observation ID and data set path on the master control node. The acquisition is started or scheduled to begin at a later time.

PAON4 instrument has been designed to survey a significant fraction of the northern sky, 3000-5000 deg², with full right ascension coverage, though a set of 24 hours constant declination scans. In fall 2016, we carried three mini surveys, observing declination ranges around the Cygnus A and Cassiopeia A bright radio sources with the FFT firmware. Details can be found in Table 2 and a more in depth analysis can be found in (Huang 2019). As mentioned above, observations from beginning of 2017 till mid 2018 were targeted to the identification of the source of the perturbations. We started the first extended PAON4 survey in July 2018, covering about 20 degree in declination, comprised between those of Cas A and Cyg A. More than forty 24 hours constant declination scans with 0.5 degree step have been done from July to December 2018. The observations have been split into two interleaved independent sets, labelled Scan_2018_A and Scan_2018_B. In each set, scans are separated by 1 degree step and the scans in B are shifted by 0.5 degree with respect to the corresponding A scan. The scan pattern for Scan_2018 (A & B) data sets is shown in Fig. 7. A number of additional problems have been identified by analysis of the Scan_2018 data, in particular imperfect packet synchronisation by the ADC boards in some cases. The 2019 observation strategy was then targeted to further investigate these problems and to precisely characterise the instrument (pointing, lobe ...) through long duration (LD), uninterrupted observations over several days. Table 2 summarises the characteristics of the different PAON4 data sets.

5 DATA PROCESSING

The data processing pipeline is composed of a set of C++ programs and python scripts which perform the tasks listed below. The input of the processing pipeline are the visibility files, containing $N_{\text{vis}} \times N_{\text{freq}}$ matrices, one matrix per visibility sampling time, where N_{vis} is the number of visi-

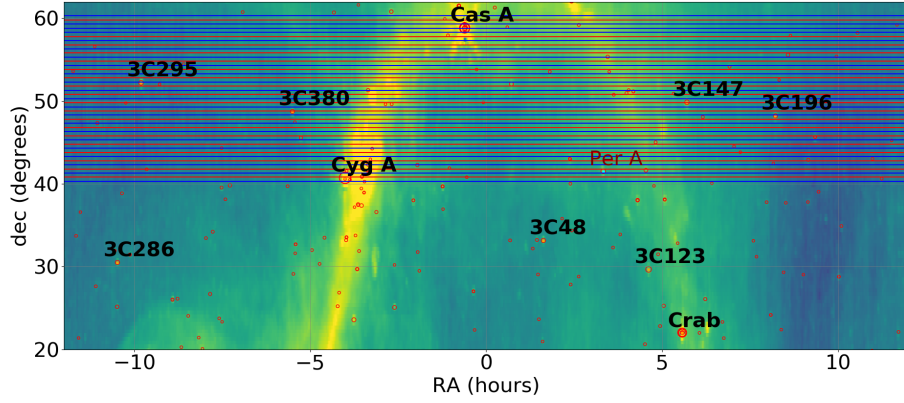


Figure 7. PAON4 acquisitions in summer and fall of 2018, in the (RA,dec) sphere with equatorial projection. Each acquisition is represented by an horizontal line, blue or red for the two halves (see text). The position of bright sources from NVSS (with the addition of Perseus A) is shown by open circles. The diameter of the circle represents the source brightness. The underlying image is a projection of the Haslam 408 MHz synchrotron map, prior to source subtraction, as retrieved from the LAMBDA archive

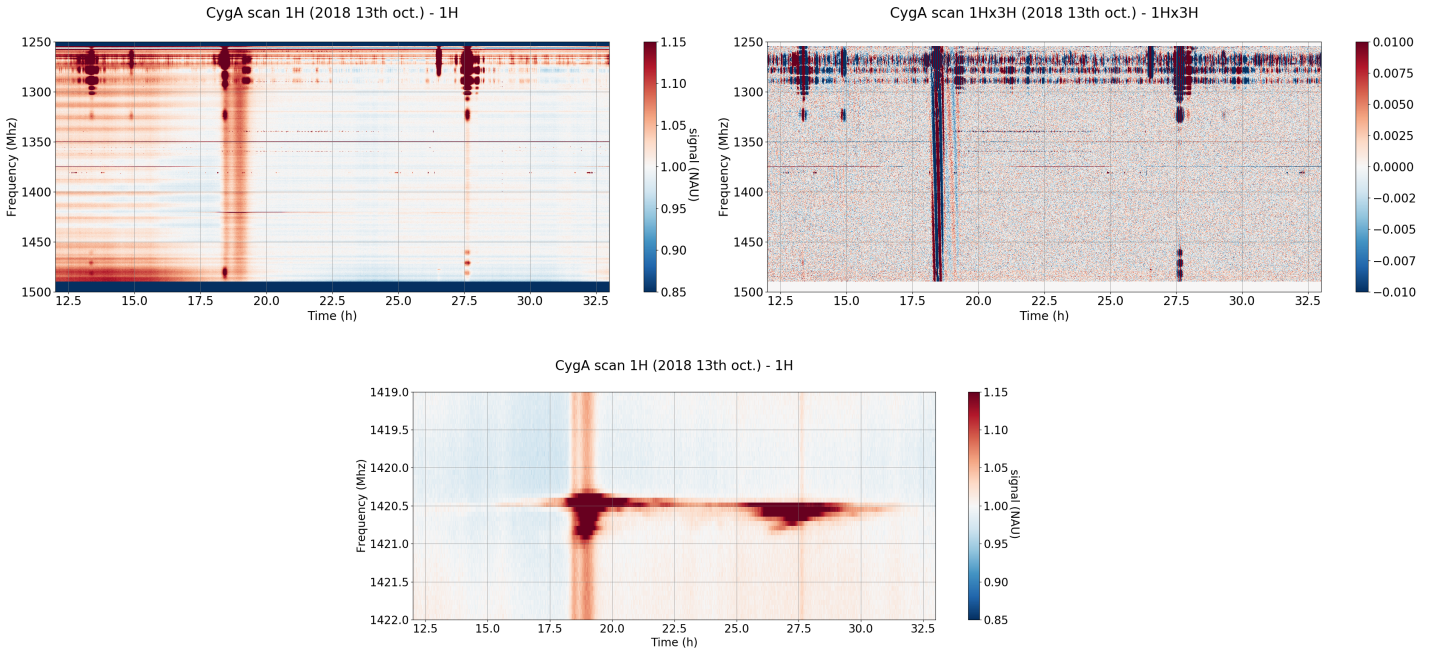


Figure 8. Top row : Examples of time frequency maps, in normalised units (NAU) obtained from processing PAON4 visibility data (after gain correction). Time (UT) is along the horizontal axis, spanning about 24 hours here, starting from 0h UT on the starting day (Oct. 13th here). The vertical axis corresponds to frequency, varying from 1250 MHz to 1500 MHz, from top to bottom. The autocorrelation signal 1H is shown on the left, while the cross correlation signal 1Hx3H is shown on the right. The transit of Cyg A can be seen at about 18h30 UT, followed by some bright galactic emission. Several satellites transits are also clearly visible, including one just before the Cyg A transit. Residual RFIs (not corrected for) and time variation of the stationary wave pattern in $g(\nu)$ before CygA transit in the autocorrelation map are also visible. Bottom row : zoom of the autocorrelation of the 1H channel around the 21 cm frequency.

bilities, and N_{freq} , the number of frequency channels, which are respectively equal to $N_{\text{vis}} = 36$ and to $N_{\text{freq}} = 4096$ for PAON4. Most of the data analysed here has a visibility sampling rate of 3 s or 6 s. The pipeline includes currently the following components:

- (i) data quality monitoring and noise characterisation
- (ii) Determine and correct for time dependent electronic gain variations $G(t)$ as well as frequency dependent gain $g(\nu)$

- (iii) Produce time-frequency binned (TFM) or right ascension-frequency binned (RAFM) maps for the different visibilities

- (iv) Perform phase and gain calibration using known sky sources, determine instrument parameters such as system temperature T_{sys} or beam response

- (v) RFI flagging and cleaning, mostly performed on TFM maps

- (vi) Produce fully cleaned and calibrated time-frequency

DataSet	Period	declination (deg)	Nb.Scans	Duration	comment
CygA-Sep16	Fall 2016	37...44	10	2 weeks	FFT firmware
CasA-Sep16	Fall 2016	56...60	5	2 weeks	FFT firmware
CygA-Nov16	Fall 2016	35...46	11	2 weeks	FFT firmware
Scan_2018 A	Summer 2018	40...60	20	~ 2 months	$\delta_{step} = 1\text{deg}$
Scan_2018 B	Fall 2018	40...60	20	~ 2 months	$\delta_{step} = 1\text{deg}$
LD_1	January 2019	25, 30, 42, 58	4	~ 10 days	CasA, CygA, M1, VirA
LD_2	April/May 2019	12...24	7	2 weeks	M1, Sun ...
LD_3	June, July 2019	35	1	10 days	CygA, stability checks
LD_4	July 2019	12, 22, 58	3	$\gtrsim 2$ weeks	CasA, M1, VirA

Table 2. PAON4 data sets

binned (TFM) or ascension-frequency binned (RAFM) maps for the different visibilities which are then used by the subsequent analysis stages, the map making in particular.

(vii) Several programs performing map making through different methods, including m-mode decomposition (see e.g. (Zhang et al. 2016b))

The mathematical formalism for radio interferometer measurement equations and the calibration methods have been studied by many authors, including polarimetry issues e.g. (Hamaker et al. 1996; Sault et al. 1996; Smirnov 2011). The numerical optimisation problem has also been studied e.g. (Salvini & Wijnholds 2014; Smirnov & Tasse 2015) as well as their application to the calibration of large arrays such as LOFAR, MWA or HERA (Kazemi et al. 2011; van Weeren et al. 2016; Byrne et al. 2019). However, specificities of mid frequency arrays operating in transit mode have not yet been fully investigated.

In this paper, we focus on the first four stages of the pipeline, listed above. The discussion of subsequent stages and the maps produced from PAON4 observations is beyond the scope of this paper, and will be the subject of forthcoming publications.

Typical time frequency maps (TFM) spanning 24 hours, obtained after a basic processing of PAON4 visibility data are shown in Fig. 8. These maps were obtained from data taken on 21018 Oct. 13th, with antennas pointed toward CygA declination at $\delta = 42^\circ$. The left panel shows the autocorrelation signal from the 1H channel where the strong pollution of the lower part of the frequency band, below ~ 1300 MHz by RFI, mostly from satellites, is clearly visible. The transit of bright sources, here CygA and Galactic plane crossing can be seen on the autocorrelation map. The Galactic 21 cm emission around 1420 MHz is also visible, with the zoom around this frequency in the lower panel showing the Galactic frequency dependent emission pattern. The right panel shows the cross-correlation signal from the (1Hx3H) feed pair. In addition to gain correction, an average frequency template, corresponding to the correlated noise has been subtracted from the cross-correlation time-frequency map. The transit of the bright source is clearly visible with high signal to noise ratio, as well as satellites in the lower frequency range.

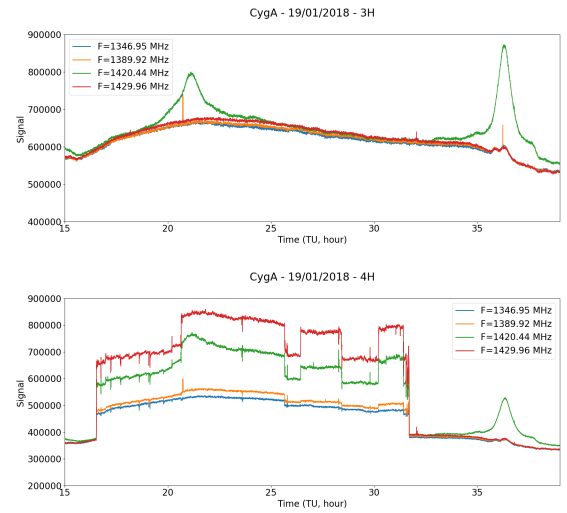


Figure 9. Example of variations of autocorrelation levels as a function of time measured on PAON4 for two channels (3H, top and 4H, bottom) on January 19th, 2018, at 4 frequencies (blue : 1347 MHz, orange : 1390 MHz, green : 1420.5 MHz, red : 1430 MHz) over a duration of about 24h. Antennas were set at the elevation of Cygnus A's transit. During this observation, channel 4H was *perturbed*.

5.1 External perturbations

Before July 2018, PAON4 data were marred with a nagging systematic perturbation. Finding its origin occupied a major fraction of PAON4 observing time in 2017 as well as during the first semester of 2018. Indeed, we were observing sudden changes in the signal level, on a few of PAON4 signals. Figure 9 shows the variations of signal levels at four frequencies, for the 3H signal on the left, with normal behaviour, and the 4H signal on the right, exhibiting sudden level changes or jumps, at all four frequencies. On the normal 3H autocorrelation signal, one may observe a slowly varying trend, which is due to temperature induced gain variations, following day-night temperature changes. The transit of Cygnus A, at about 36h (i.e. 12h TU), is visible on all frequencies excepted at 1420.44 MHz where 21 cm Galactic emission dominates. In contrast with this normal behaviour, the perturbed 4H signal exhibits erratic variations, from a sharp rise at about 17 h and ending after a sharp fall at about 32 h (8 h next day),

with several intermediate positive or negative steps, at all frequencies. Such perturbation were already seen on early PAON4 data, in 2015, but were more frequent during the 2017-2018 year. Investigating this effect during that year, we noted that :

- the perturbation occurrence rate was of about 80% (i.e. 8 days out of 10),
- only one antenna was affected at a time,
- the most affected antenna was antenna 4, with a rate of about 80%. However, in 2015, whenever the effect was observed it affected only antenna 3,
- in the rare occurrences where one of the another antennas was affected, both polarisations were affected by similar (but not identical) perturbations, in exactly the same time interval. In the case of antenna 4, one of the two polarisation probes on the feed, the 4V channel, was blinded, from mid 2016 to mid 2018, by a $50\ \Omega$ resistor connected to the LNA's input. No significant perturbation was ever observed on the the blinded channel.

This last fact, combined with other checks through electronic modules and cables permutation showed that the perturbation had an external origin. Accumulating more data along the year brought another intriguing piece of evidence, displayed in Fig. 10. The start and end times of the perturbation seemed to correlate quite well with the hour of the dawns and sunsets in Nançay, although with some dispersion. After a long investigation campaign, we finally spotted in May 2018 a small bird spending its nights in the shielded environment of the chokes surrounding our feed. We concluded that the thermal radiation produced by the bird was the source of an additional signal during the night. Anyhow, we placed anti-bird nets around the chokes end of May 2018 which definitely cured the problem.

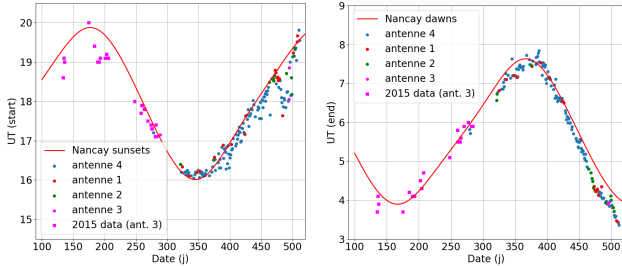


Figure 10. Variation of the starting time (left) and end time (right) of the perturbation with the date. The abscissa shows the date, reported as a number of days since January 1st, and the ordinate correspond to the time in hours. The color of the symbols correspond to the antenna which was perturbed at each date. Early PAON4 data, in April-May 2015, when only antenna 3 was perturbed, is shown as squares.

5.2 Spectral response and time dependent gain

The PAON4 channels response varies both with time and frequency. We use in our analysis a simplified gain correction model by considering these two effects independently of each other, writing $G(t, \nu) = G(t) \times g(\nu)$.

As a result of the combination of the various stages of

frequency filtering, and signal transmission cables, the frequency response is complex (Fig. 11). The gain $g(\nu)$ shape is firstly determined by the LNA and pre-amplifiers spectral response but in the current design of the DAQ, the 50 m coax cables between the central dish and the digitisation boards located in the EMBRACE container are responsible of the dramatic gain decrease above 1300 MHz. For each channel, the gain also presents specific wiggles that we attributed to standing waves in the 9 m cable between the LNA and the pre-amplifier and the 10 m cables between the pre-amplifier and the local oscillator electronics. The characteristics of these standing waves are time variable. The peak-to-peak wave separation, of the order of 12.5 MHz, is inversely proportional to the cable length which first has motivated to shorten the cables as much as possible with the present analogue electronic design, and secondly to engage a R&D program with the aim of performing the analogue to digital conversion as close as possible to the LNA on the feed. This R&D program will lead by the spring of 2020 to the installation of new electronic boards called IDROGEN (see Section 7).

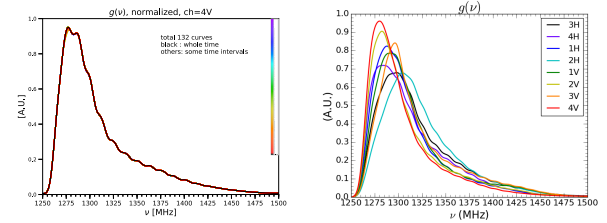


Figure 11. Frequency dependent gain determination from November 2016 data. Left: stability of the frequency dependent gain $g(\nu)$ over time. The 4V channel gain is shown, with the total time interval split into 131 intervals. The black curve shows the $g(\nu)$ for the whole period, while gain for the 131 intervals are shown in different colors. Right: the normalised frequency dependent gains $g(\nu)$ for the eight PAON4 RF signals.

As already mentioned above, in section 5.1, and shown in Fig. 9 (right hand side), the raw PAON4 auto-correlation signal levels present in each channel a systematic drift in time, with a day-night pattern. This has been attributed to the overall analogue electronic chain gain variations with the ambient temperature. Indeed, the analogue electronic is located outside, without any environmental control system. The temperature stability of PAON4 electronic chain has been measured in the lab, and we have found 4 dB ($\sim 60\%$) gain variation for temperature varying between 0°C and 55°C . In the PAON4 set-up, the analogue electronic being located outside, a 15°C range would be common, and with the sun shine effect, the daily amplitude of the temperature variation can easily reach and exceed 30°C , leading to $\sim 30\%$ gain variations.

Using data taken in 2017 and 2018, with blinded 4V channel, we have been able to show that time variation of the signal of each channel, outside bright sky source transits times, was tightly correlated with the blinded channel. A gain variation model based on this correlation was then created and the blinded channel signal used to compute and correct for the time varying gain term $G_i(t)$ of all other channels. The effect of gain variations have been decreased

from $\sim 25 - 30\%$ to $\pm 3 - 5\%$ using this simple scheme. The 4V channel has been unblinded in July 2018, and an additional blind channel, THERMON, has been added to PAON4, which has been subsequently used to correct for gain variations. The gain corrected visibilities are expressed in NAU (*Normalised Arbitrary Unit*), with auto-correlation levels close to unity outside bright sources or sky transits.

We determined for each channel the parameter of a linear correlation with the median of the signal (after satellites and sources removal) and the THERMON signal (in the same time frame). We show in Fig. 12 examples of this reconstruction for the 1H channel, when analysing data from the Scan_2018 A and B part simultaneously. A unique slope was fitted, with different intercepts for each observation run. Once correcting for the linear variations, outlined in cyan, the signal variation amplitudes are reduced from $\sim 25 - 30\%$ to $\pm 3 - 5\%$. As also shown on the right panel of this figure, while the THERMON and the antennas channels are both correlated with a direct temperature measurement, this correlation has a large dispersion and shows hysteresis as a result of the different mechanical structure and positioning of the temperature sensor (on top of the EMBRACE hut). Figure 12 shows that THERMON signal provides a better template for correcting the temperature-induced signal variations, than a direct temperature measurement. Hints of a residual hysteresis may be seen on the left panel, which could be explained by the thermo-mechanical differences between the LNA's on the feeds and the lighter THERMON set-up, leading to faster temperature variations for the latter.

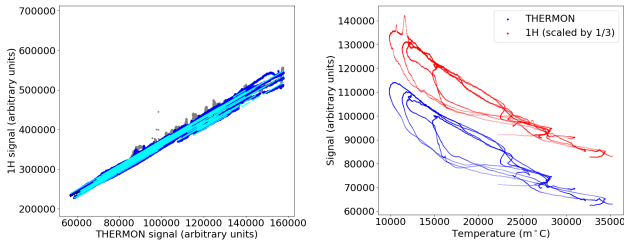


Figure 12. Left: figure illustrating time dependent gain $G(t)$ correction, for channels 1H, for good data from Scan_2018 A and B. Gray dots are excluded from the fits (due to source transit, satellites or RFIs), only those blue ones are used. The cyan thin lines represent the results of the global fit, with one slope for all datasets but one intercept for each of the observation runs. Right: variations of the THERMON and 1H channels as a function of the measured ambient temperature, along the horizontal axis, over a few days in July 2018.

5.3 On sky calibration

We have used known point sources on sky to determine the instrumental phases, as well as the antenna beam and overall radiometric calibration. The PAON4 survey strategy includes regular observation of bright sky sources, such as Casiopeia A (Cas A) and Cygnus A (Cyg A), every few days to obtain gain and phase calibration parameters which are then used for the subsequent scans and update the instrument model. Our primary calibration source is Cas A which can be considered as a point source for PAON4. A simple model can be used to represent expected auto-correlation

and cross correlation signals from Cas A, and we fit instrumental phases, amplitudes, as well as beam shape parameters and a shift in the pointing direction along the East-West direction on the auto-correlations and cross correlation signals, separately for the H and V polarisations. For each polarisation, H or V, independently from each other, the parameters are adjusted on the set of 4 auto-correlations and 6 cross-correlations signals, for each binned frequency channel separately. The cross-correlations between two orthogonal probes $H \times V$ haven't yet been considered, ignoring source polarisation. After fitting the auto-correlations which notably fix the beam shape parameters, the 6 cross-correlations signals are used to determine relative phases between the feed on antenna 1 taken as reference and the 3 other feeds (i.e $\Delta\Phi_i = \Phi_i - \Phi_1$ with $i = 2, 3, 4$). There are degeneracies between the instrumental phases and the relative phases induced by the array geometry, which is fixed at this stage. We have however tried to refine PAON4 antenna positions, determined from geometrical measurements during PAON4 deployment, using satellite transits as described below.

As mentioned earlier, the lower part of PAON4 band, below 1300 MHz is heavily polluted by satellite emissions, dominated by positioning satellites from the GPS (US), Galileo (EU) and Beidou (China) constellations. In particular, PAON4 sees a strong signal from Galileo E6 band, centred at 1278.75 MHz, as well as from Beidou in the same band. Although GPS do not have direct emission in PAON4 band (1250 – 1500 MHz), we do see the GPS L2 signal centred around 1227 MHz, at the symmetric frequency of ~ 1273 MHz, with respect to the LO frequency at 1250 MHz. It was realised that these satellite signals could also be used for determining PAON4 geometry, beam shape and instrumental phases, as several satellite tracks are usually present in our daily (24 hours) observations. We developed an additional software module included in our pipeline which uses satellite tracks, computed using the SGP4⁴ library from NORAD⁵ TLEs (Two Line Elements) available from CELESTRAK⁶, as well as celestial objects tracks, at different frequency, separately for each polarisation, and performs the following operations:

(i) Determine the pointing directions, as well as parametrised beam shape for each PAON4 antenna, using auto-correlation signals and the satellite tracks. It should be noted that the satellite signals are very strong, Galileo satellites appear as few hundred times brighter than Cas A.

(ii) Using the parameters determined above, the phases are determined for each baseline separately. It is also possible to determine the phases from combined fit over the six baselines and multiple frequencies, using a linear frequency dependent phase model $\Phi_{ij}(\nu)$.

(iii) We have used instrumental phase variations with pointing directions to refine PAON4 antenna positions along the vertical direction (Oz) and the North-South directions, as discussed below in section 6. The positions along the East-West direction changes the fringe rate and a combined fit,

⁴ <https://www.danrw.com/sgp4/>

⁵ <https://www.norad.mil>

⁶ <http://www.celestrak.com/NORAD/elements>

using visibility data from different declinations and many sources can be used to obtain precise array geometry.

(iv) Among the fitted parameters are the source amplitudes. We have used the source amplitudes for Cas A and Cyg A to determine PAON4 radiometric calibration factors (Kelvin/NAU), to convert gain corrected visibilities to temperature. Instrument gain stability is also discussed in section 6.

6 INSTRUMENT PERFORMANCE

This section presents some of the results obtained from partial analysis of PAON4 data, taken in fall 2016 and then, in fall 2018, winter and spring 2019. Some of the aspects concerning the overall instrument performance, as well as calibration parameters precision and stability is discussed here.

6.1 System temperature and radiometric calibration stability

To determine the antenna temperature of the 8 polarizations (i.e. H and V types), during the observation period at several times, we have used the transit of the Cas A and Cyg A bright sources as well as some satellite transits. Two procedures have been used, the first one (a) uses satellite tracks and CasA and CygA transits and have been applied to data from 2019 long duration LD observations. The dish diameter in this procedure is determined from the autocorrelation signals using satellite transits, while the bright source maximum amplitude N_{ij} is obtained from fitted the cross-correlation signal between two same polarisation signals (ie. H-H or V-V cross-correlation only). In the second procedure (b), the auto-correlations signals during the CasA transit have been used to extract at once the maximum signal amplitude N_i and the effective dish diameter D_i for a given dish and polarisation. This second procedure has been applied to the Cas A transits during the Scan2018 (A,B) periods (Table 2). We have used a gaussian beam approximation in the procedures, and have used time-frequency maps produced after the gain $e g(\nu) \times G(t)$ correction, which lead to gain corrected autocorrelation signal levels outside the source or satellite transits very close to 1 NAU.

To convert the fit outcomes in term of radiometric calibration coefficients C^{Jy} in Jy/NAU and C^K in Kelvin/NAU, we have used the CasA and CygA spectral flux reported in reference (Perley & Butler 2017) which gives for CasA an intensity of $I_s = 1730$ Jy and $I_s = 1772$ Jy at 1440 MHz and 1396 MHz respectively, and for CygA an intensity of $I_s = 1585$ Jy at 1396 MHz. The expression of the radiometric calibration coefficient C^K , to convert normalised units NAU to temperature in Kelvin, derived from the source intensity I_s can be then written as:

$$C_i^K = \frac{I_s}{2N_i} \frac{\pi}{4k_B} D_i^2 \quad \text{K/NAU} \quad (1)$$

The signal levels being around 1 NAU outside sources, the value of this calibration coefficient is also equal to the system temperature T_{sys} reported in Table 3. We have used two procedures applied to different data sets to determine

effective dish diameters and radiometric calibration. Procedure (a) operates at 1396 MHz and uses the satellite tracks to fit the effective dish diameters and the radiometric calibration is then determined from fitting the 12 cross-correlation maximum intensities during the bright sources transits. This procedure has been applied to Cas A and Cyg A transits separately, during a single, although long period of observation. Procedure (b) operates at 1440 MHz and fit at once the maximum intensity of the 8 auto-correlations during the eight Cas A transits, with observations scattered over several months. The estimated relative uncertainty on the system temperature is approximately 10% and few percent for the diameters.

We also note that the effective diameter shows a variation with respect to the frequency due to standing waves between the reflector and the feed. The two frequencies chosen experimentally correspond to the location of nodes of these standing waves. Table 3 summarizes the different values of the antenna temperatures and effective diameters. We estimate a relative uncertainty of 10% mainly due to the maximum intensity and the effective diameter errors, leading to a stability level better than 10% on the instrument radiometric from the measurements performed over several months. The results show a tendency for the dish number 4 to be more noisy which may be due to the fact that this dish is the closest to the surrounding trees, and with the fact that the H type polarisation feeds are about 20% noisier than the V-polar feeds ($H : T_{sys} \sim 130$ K, $V : T_{sys} \sim 110$ K). The origin of this difference between H and V feeds hasn't yet been understood.

Further studies has to be done to clarify the source of additional contributions, leading to a total noise temperature of ~ 120 K, starting from $\sim 60 - 70$ K electronic noise (see section 3.1). Inefficiencies of the mesh reflector, leading to a partial shielding of the ground thermal emission can be one of the sources of this noise excess.

6.2 Noise characterisation

Given the $\sim 10^5$ ratio between the noise level and the expected cosmological 21 cm signal, which is essentially stochastic, characterising the noise and the way fluctuations decrease with integration time is a central question for IM mapping instruments. Interferometry has the intrinsic advantage of being rather immune to variations of individual receivers noise levels, however, correlated noise would limit the theoretical sensitivity expected from combination of visibility signals, with long integration time. Moreover, interferometric arrays designed for IM surveys are closely packed, which increases the concern for the correlated noise between receivers, due to electromagnetic coupling between feeds. We have studied the noise behaviour of our complete electronic chain, including the digitiser boards in laboratory, and identified some coupling sources, responsible for correlated noise, such as the coupling through the power supplies. For more than a year, till July 2018, data has been taken with a blind 4V signal, where the input of the amplifier on the 4V feed was connected to a 50Ω resistor. These data have been used to help identify the sources of various perturbations, including the ones subsequently identified as being due to a bird, control gain variations. They have also been used to study the correlated noise, comparing visibilities involving the 4V

Table 3. Results on system temperature and effective diameter determined for each of the 8 polarizations using different two different procedures (a) and (b) described in the text.

Polar.	$T_a^{CasA}(K)$ (a)	$T_a^{CygA}(K)$ (a)	$D^{CasA}(m)$ (a)	$D^{CygA}(m)$ (a)	$T_a^{CasA}(K)$ (b)
1H	116	147	4.03	4.35	144
2H	127	129	4.12	4.38	133
3H	130	122	4.05	4.28	138
4H	161	152	4.17	4.21	185
1V	113	100	4.30	4.08	103
2V	108	92	4.27	4.18	100
3V	103	111	4.33	4.07	98
4V	143	151	4.38	4.00	180

signal with other signal pairs. Our conclusions, from a preliminary study of the correlated noise, are summarised below. We have used data from January 2018 observations, and computed time frequency maps, with $\delta\nu \simeq 500$ kHz frequency resolution and 12 minutes time bins, corresponding to an effective per pixel integration time of $\Delta t \sim 50$ s. Dispersions on the visibility signals (real/imaginary parts) have been then computed over clean sections of the TFM maps, covering ~ 6 hours in time and ~ 35 MHz, outside bright regions of the sky. A noise reduction factor $\sqrt{\Delta t \times \delta\nu} \sim 5000$ is expected. The r.m.s. (σ) values quoted below assume that the signals have been normalised to get auto-correlations levels equal to unity, outside bright sources, and r.m.s values should be scaled with the noise temperature $T_{sys} \sim 120$ K to convert them to temperatures.

- The noise level observed for signal pairs involving the blinded 4V signal (1V-4V, 1H-4V ...) are compatible with the levels expected given the integration time and frequency bandwidth, leading to $\sigma_{re,im} \sim 2. \times 10^{-4}$. The correlated noise contribution could be considered negligible, at least for the integration times of the current analysis.

- For the same polarisation signal pairs between two different dishes, such as (1H-3H) or (1V-3V), the observed noise level is higher compared to the expected level, assuming gaussian uncorrelated noise. We measure dispersions up to 4-5 times higher, $\sigma_{re,im} \sim 8. \times 10^{-4}$.

- For two cross polarisation probes located in the same feed/dish such as (1H-1V) or (3H-3V), the dispersion level increases to more than $\sigma_{re,im} \sim 2.10^{-3}$.

The observed extra noise observed on the same polarisation probes in two different feeds, or two probes within the same feed shows up as frequency dependent patterns, quite stable in time over few hours. It can be interpreted as noise generated in the analogue electronic chain, cross fed through electromagnetic couplings between feeds on two different dishes, or between probes in the same feed, and then amplified in a way analogous to the Larsen effect. Fortunately, it can efficiently be subtracted thanks to its stability in time. Further studies are needed to determine the noise floor due to this correlated noise.

We have also analysed how the noise level decreases with the integration time. Here, time frequency maps with different effective per pixel integration time are computed, with

a fixed frequency bin width $\delta\nu = 500$ kHz, from April-May 2019 data. Maps with different averaging time window sizes, equal to (1,2,4,8,16,32,64,128) in units of visibility sampling time have been built and then used to compute signal dispersions (in the absence of bright source transits or RFIs). Spring 2019 data was taken with a visibility sampling time of 6 s, leading to a maximum visibility averaging time of 768 s. However, bearing in mind that PAON4 was operated with $\sim 10\%$ on sky efficiency, the maximum effective integration time would be slightly above one minute. Figure 13 shows the evolution of the dispersion levels, computed as the r.m.s. of the different time-frequency maps, excluding bright sources, satellites and RFI. The correlated noise has been subtracted from the cross-correlations time-frequency maps, as the frequency template obtained by the time averaged signal, computed separately for each cross-correlation. The left panel shows the evolution of the dispersion with the integration time, for the 8 PAON4 autocorrelation signals. The r.m.s. decreases with the integration time, following the $1/\sqrt{\Delta t}$ trend. A noise floor or saturation starts to appear at long integration times, more or less strongly depending on the data set and the auto-correlation signal. However, it should be kept in mind that the r.m.s of the autocorrelations signals we recover is sensitive to gain variations with time, as well to the variation of the diffuse sky brightness. The presence of such apparent noise floor for the autocorrelation signals does therefore not imply that the underlying noise is not white. The right panel shows the evolution of the r.m.s. values computed on the cross-correlations visibilities (real part) for the 12 H-H and V-V correlations. Here, the r.m.s. values are compatible with the expected levels, and decrease with integration time following the expected white noise law $1/\sqrt{\Delta t}$, without significant contribution from correlated noise, once the average level at each frequency has been subtracted.

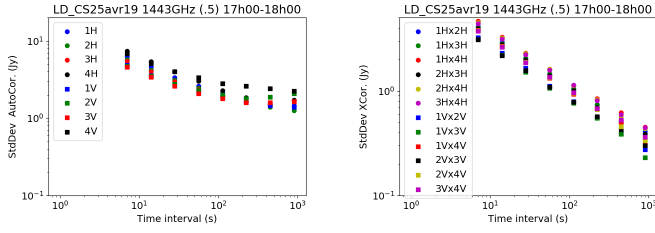


Figure 13. Evolution of noise level with integration time. Left: dispersion level for the eight PAON4 autocorrelation signals, as a function of the integration time. Right: dispersion level for the real parts of the 6 H-H and 6 V-V cross correlations signals, as a function of integration time in seconds.

6.3 Phase calibration and array geometry

As explained in section 5.3, we have used Galileo satellites to perform phase calibration and determine instrumental phases, for a large fraction of PAON4 observations carried in fall 2018, winter and spring 2019. Instrumental phase values are determined for each constant declination scan. The left panel in Fig. 14 shows the antenna 2 phase $\Delta\Phi_2 = \Phi_{12} = \Phi_2 - \Phi_1$ values, determined at 1278.5 MHz for 17 scans and the H-polarisation feeds, as a function of the common, nominal antennae direction in the meridian plane, referred to as the Zenith angle ($Z = 90^\circ - \text{elevation}$). This angle corresponds to the angle between antenna axis and the local vertical, or the difference between the observed declination and the instrument latitude. Negative zenith angles correspond to antennae tilted toward the south. One can see that the phase Φ_{12} varies over more than 30° , with a smooth variation as a function of the zenith angle. The variation is well accounted for by a shift in theoretical antennae position, along the north-south Oy and vertical Oz directions. The fitted best model, taking into account the baseline shift is shown as the red curve. The fit result shows that the two feed heights differ by about ~ 55 mm for this (1H-2H) baseline, while the north-south component of this baseline should be corrected by ~ 14 mm. Using the six baselines, we have determined the corrections to the array geometry, using the zenith dependency of the instrumental phases. We obtain precisions about ~ 2 mm using these 17 scans. A shift in the east-west baseline component would not show as a zenith angle phase dependency, but rather as a change in the fringe rate. We haven't yet tried to determine baseline corrections along the east-west Ox direction using the fringe rates, but higher precision is expected for the determination of the east-west baseline corrections. The right panel in Fig. 14 shows the result of the phase calibration for the same (1H-2H) baseline. The instrumental phases do not change by more than $\sim 5^\circ$, despite the fact that the observations have been carried over a period spanning more than 8 months. Similar phase stability is observed for the other baselines.

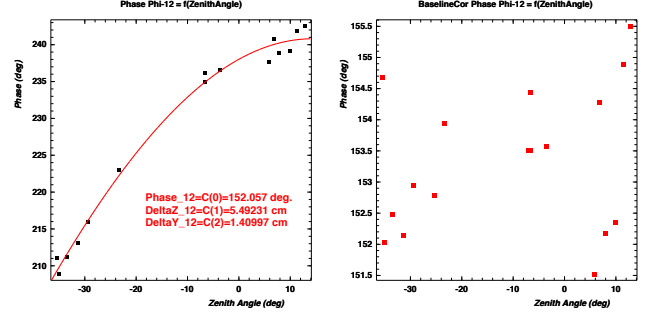


Figure 14. Phase calibration and array geometry corrections. Left: Instrumental phase values Φ_{12} determined for different scans, plotted as a function of the zenith angle (black squares). The red line represent a model fit, including corrections to the baseline. Right: Φ_{12} phase values, as a function of zenith angle, determined after correcting the baselines.

6.4 Comparison of observed and expected signals

A comparison of observed and expected visibilities for few scans close to two bright sky sources, CasA (~ 1700 Jy) and 3C196 (~ 15 Jy), is shown in Fig. 15 for the cross-correlation of two pairs of feeds, 1H-2H and 2H-3H. We gathered data from scans at several declinations around the source, represented in different colors. The visibility amplitude decreases for scans at more distant declinations with respect to the source declination. This effect is clearly visible for CasA source, but also for 3C196. The expected signal was rescaled using a single conversion coefficient per feed, used for both sources, computed by adjusting the amplitudes of the expected CasA on the source scan of July 17th, 2018. This simplified computation of expected signals does not take into account pointing uncertainties, whereas a ~ 0.5 deg shift is suggested by our satellite fits, nor for the non-gaussian secondary lobes in the beam pattern. The full signal levels for CasA is expected to be about ~ 6000 mK, and ~ 60 mK for 3C196, while the noise level is about ~ 20 mK given the time and frequency binning used here.

Figure 16 shows a region of the reconstructed map at 1400 MHz, from PAON4 observations carried in fall 2016 (November 16th to December, 1st 2016), using m-mode decomposition in harmonic space (Huang 2019). A sky map covering the full 24 hours right ascension, and the declination range $35^\circ \lesssim \delta \lesssim 46^\circ$ has been computed from eleven (11) 24-hours constant declination scans around Cygnus A declination. The extracted map covers a $\sim 18^\circ$ in declination ($32^\circ < \delta < 50^\circ$) and $\sim 35^\circ$ in right ascension ($290^\circ < \alpha < 325^\circ$) around the nearby radio galaxy Cygnus A. The emission from Cyg A, the Milky Way synchrotron emission, as well as from Cygnus X star forming region is clearly visible.

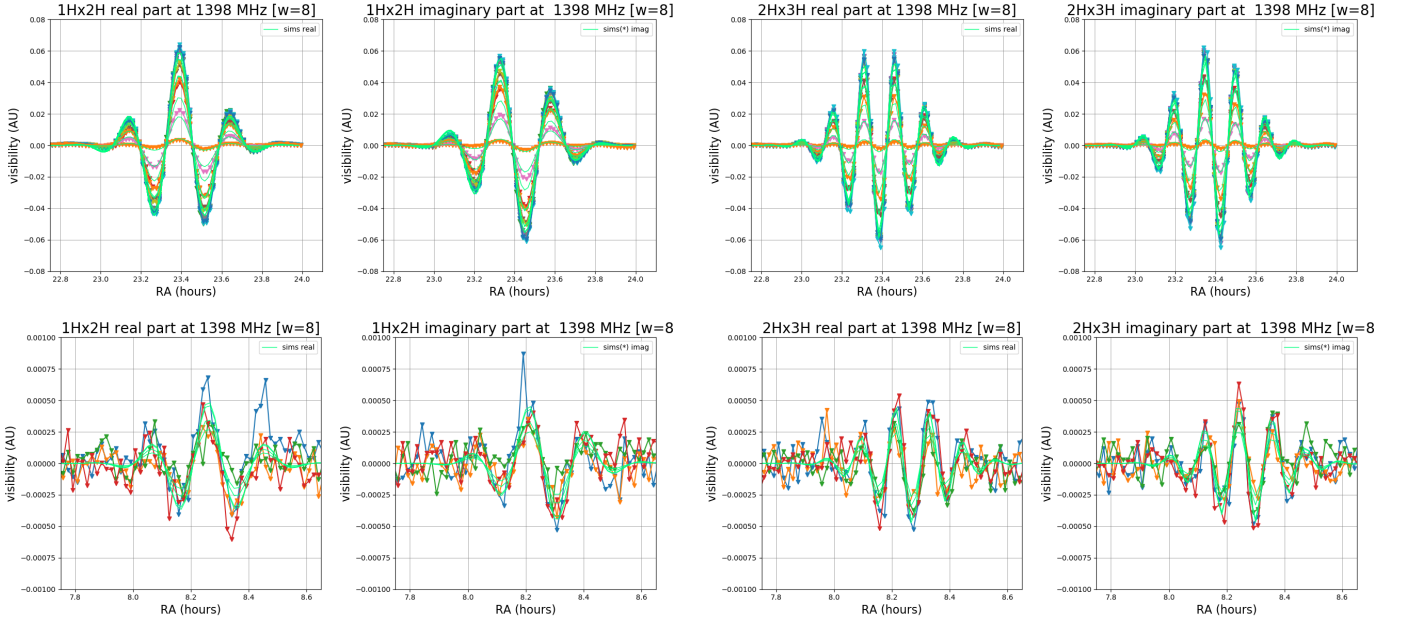


Figure 15. Comparisons of observed and expected (with a simplified model, see text) visibility variations with right ascension for scans near CasA (top) and 3C196 (bottom) declinations, from the Scan_2018 A and B data, for the 1H-2H (left) and 2H-3H (right) cross-correlations. Each color correspond to a different date, and the expected visibilities are shown in cyan.

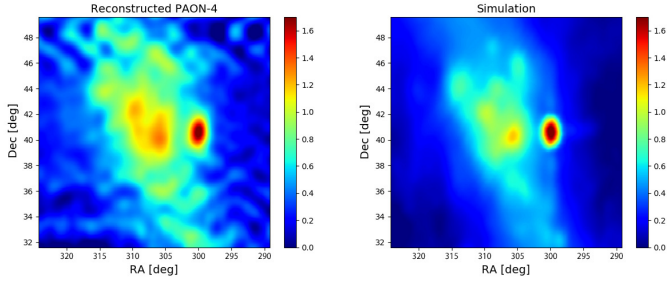


Figure 16. Example of a reconstructed map, in a $\sim 35^\circ \times 18^\circ$ region around Cygnus A, covering the area ($32^\circ < \delta < 50^\circ$) in declination and ($290^\circ < \alpha < 325^\circ$) in right ascension, from November 2016 PAON4 data (left). Right panel shows the simulated map, as would be seen by PAON4. (Huang 2019)

7 FUTURE PROSPECTS

As mentioned in Section 5.2, time-variable systematics in the frequency response led us to develop a new generation of sampling and signal processing board, IDROGEN/NEBuLA, to perform digitisation as close to the feeds as possible. The IDROGEN board has been designed to equip interferometers with several hundred feeds, scattered over few hundred meters, thanks to its implementation of the White Rabbit⁷ technology for clock synchronization. A first version of this new board, called NEBuLA (NumEriseur a Bande Large pour l’Astronomie) was designed and produced in 2016-2017. The second version, now called IDROGEN, is being developed as part of the CNRS/IN2P3 DAQGEN

project. This project, started in 2017, aims at developing generic modules for rapid acquisition systems for particle and astro-particle projects.

IDROGEN boards will be located in the electronic boxes on each antenna, sampling the RF signals, relieving the need for frequency shifting, and transmitting the digital streams over optical fibres all the way to the computer cluster, few hundred meters away. The deployment of IDROGEN boards on PAON4 is foreseen in spring 2020, after more in-depth characterisation of PAON4 in its present configuration.

Upgrades of the acquisition system hardware and software are also planned, and should enable PAON4 to reach $\sim 25\%$ to 30% live time on the sky (instead of $\lesssim 10\%$ now, see Section 3) after the deployment of IDROGEN boards. In particular, GPU support will be added to the TAcq package, at least to the correlation computing software processor, and very likely to the FFT processor to increase the system throughput. First tests will be performed while staying in the operation mode currently in use in PAON4, which was also intended to prepare for the deployment of the new IDROGEN digitiser boards. At a later stage, the new digitiser boards will also be operated and qualified in the FFT mode. We plan to release a stable version of the TAcq software, with full support for IDROGEN boards, after those tests.

8 CONCLUSIONS

Densely packed dish array interferometer might be a cost effective option to build radio instruments to survey large sky areas in L-band. We have build and operated the PAON4 dish array transit interferometer under very tight budget constraints. Preliminary results, discussed in this paper in-

⁷ <https://white-rabbit.web.cern.ch>

dicating that this type of instrument and associated observing strategy are indeed applicable and cost effective. The study presented here needs however to be continued to get to much higher integration time, to assess that the expected sensitivities at a few mK level can indeed be reached. More in depth studies with more data and PAON4 maps will be published in the coming year. PAON4 does not have redundant baselines, and the additional possibilities offered by the combination of nearly identical baselines has to be explored with larger instruments. Such studies are being pursued in parallel with the Tianlai dish array. The next generation IDROGEN digitiser/signal processor boards are in the final stage of development and will be suited for dish interferometer with up to few hundred feeds, with up to \sim km baselines. IDROGEN will be deployed for qualification on PAON4 in 2020 and we plan to carry a higher sensitivity survey in the declination range $30^\circ \dots 60^\circ$ in 2021.

ACKNOWLEDGEMENTS

The deployment of PAON4 and observations at Nançay would not have been possible without the help and support of the technical staff of the Nançay Radio Observatory, which is the Unité scientifique de Nançay (USN) of the Observatoire de Paris, associated as Unité de Service et de Recherche (USR704) to the French Centre National de la Recherche Scientifique (CNRS). The Nançay Observatory also gratefully acknowledges the financial support of the Conseil régional of the Région Centre in France. We acknowledge financial support from "Programme National de Cosmologie and Galaxies" (PNCG) of CNRS/INSU, France.

REFERENCES

- Abbott T. M. C., et al., 2018, *MNRAS*,
 Abdalla F. B., Rawlings S., 2005, *MNRAS*, **360**, 27
 Amendola L., Kunz M., Motta M., Saltas I. D., Sawicki I., 2013, *Phys. Rev. D*, **87**, 023501
 Ansari R., Le Goff J., Magneville C., Moniez M., Palanque-Delabrouille N., Rich J., Ruhlmann-Kleider V., Yèche C., 2008, preprint, ([arXiv:0807.3614](#))
 Ansari R., Campagne J.-E., Colom P., Magneville C., Martin J.-M., Moniez M., Rich J., Yèche C., 2012a, *Comptes Rendus Physique*, **13**, 46
 Ansari R., et al., 2012b, *A&A*, **540**, A129
 Ansari R., Campagne J. E., Colom P., Ferrari C., Magneville C., Martin J. M., Moniez M., Torrentó A. S., 2016, *Experimental Astronomy*, **41**, 117
 Armstrong R., Hickish J., Zarb Adami K., Jones M. E., 2009, in *Wide Field Astronomy & Technology for the Square Kilometre Array*. p. 45 ([arXiv:0912.0380](#)), [doi:10.22323/1.132.0045](#)
 Bandura K., 2011, PhD thesis, Carnegie Mellon University
 Bandura K., et al., 2014, in *Ground-based and Airborne Telescopes V*. p. 914522 ([arXiv:1406.2288](#)), [doi:10.1117/12.2054950](#)
 Bandura K., et al., 2019, arXiv e-prints, [p. arXiv:1907.12559](#)
 Battye R. A., Browne I. W. A., Dickinson C., Heron G., Maffei B., Pourtsidou A., 2013, *MNRAS*, **434**, 1239
 Betoule M., et al., 2014, *Astron. Astrophys.*, **568**, A22
 Bigot-Sazy M. A., et al., 2015, *MNRAS*, **454**, 3240
 Bigot-Sazy M.-A., et al., 2016, in Qian L., Li D., eds, *Astronomical Society of the Pacific Conference Series Vol. 502, Frontiers in Radio Astronomy and FAST Early Sciences Symposium 2015*. p. 41 ([arXiv:1511.03006](#))
 Braun R., Bourke T., Green J. A., Keane E., Wagg J., 2015, *Advancing Astrophysics with the Square Kilometre Array (AASKA14)*, [p. 174](#)
 Bull P., Camera S., Raccanelli A., Blake C., Ferreira P., Santos M., Schwarz D. J., 2015a, *Advancing Astrophysics with the Square Kilometre Array (AASKA14)*, [p. 24](#)
 Bull P., Ferreira P. G., Patel P., Santos M. G., 2015b, *ApJ*, **803**, 21
 Bull P., et al., 2016, *Physics of the Dark Universe*, **12**, 56
 Byrne R., et al., 2019, *ApJ*, **875**, 70
 Chang T.-C., GBT-HIM Team 2016, in *American Astronomical Society Meeting Abstracts #227*. p. 426.01
 Chang T.-C., Pen U.-L., Peterson J. B., McDonald P., 2008, *Physical Review Letters*, **100**, 091303
 Chang T.-C., Pen U.-L., Bandura K., Peterson J. B., 2010, *Nature*, **466**, 463
 Charlet D., et al., 2011, *IEEE Transactions on Nuclear Science*, **58**, 1833
 Chen X., 2012, in *International Journal of Modern Physics Conference Series*. pp 256–263 ([arXiv:1212.6278](#)), [doi:10.1142/S2010194512006459](#)
 Cosmic Visions 21 cm Collaboration et al., 2018, arXiv e-prints,
 DES Collaboration et al., 2018, arXiv e-prints,
 Das S., et al., 2018, in *Millimeter, Submillimeter, and Far-Infrared Detectors and Instrumentation for Astronomy IX*. p. 1070836 ([arXiv:1806.04698](#)), [doi:10.1117/12.2313031](#)
 Deschamps H., et al., 2013, *IEEE Transactions on Nuclear Science*, **60**, 3620
 Furlanetto S. R., Oh S. P., Briggs F. H., 2006, *Phys. Rep.*, **433**, 181
 Hamaker J. P., Bregman J. D., Sault R. J., 1996, *A&AS*, **117**, 137
 Hinshaw G., et al., 2013, *ApJS*, **208**, 19
 Huang Q., 2019, PhD thesis, Paris-Saclay University & University of Chinese Academy of Science
 Kazemi S., Yatawatta S., Zaroubi S., Lampropoulos P., de Bruyn

- A. G., Koopmans L. V. E., Noordam J., 2011, *MNRAS*, **414**, 1656
- Masui K. W., et al., 2013, *ApJ*, **763**, L20
- Newburgh L. B., et al., 2016, in *Ground-based and Airborne Telescopes VI*. p. 99065X ([arXiv:1607.02059](#)), [doi:10.1117/12.2234286](#)
- Parsons A. R., et al., 2010, *AJ*, **139**, 1468
- Perley R. A., Butler B. J., 2017, *The Astrophysical Journal Supplement Series*, **230**, 7
- Peterson J. B., Bandura K., Pen U. L., 2006, *arXiv Astrophysics e-prints*,
- Peterson J. B., et al., 2009, in *astro2010: The Astronomy and Astrophysics Decadal Survey*. ([arXiv:0902.3091](#))
- Planck Collaboration et al., 2016, *A&A*, **594**, A13
- Planck Collaboration et al., 2018, *arXiv e-prints*, p. [arXiv:1807.06209](#)
- Pober J. C., et al., 2014, *ApJ*, **782**, 66
- Pritchard J. R., Loeb A., 2008, *Phys. Rev. D*, **78**, 103511
- Salazar-Albornoz S., et al., 2017, *MNRAS*, **468**, 2938
- Salvini S., Wijnholds S. J., 2014, *A&A*, **571**, A97
- Sault R. J., Hamaker J. P., Bregman J. D., 1996, *A&AS*, **117**, 149
- Shaw J. R., Sigurdson K., Pen U.-L., Stebbins A., Sitwell M., 2014, *ApJ*, **781**, 57
- Shaw J. R., Sigurdson K., Sitwell M., Stebbins A., Pen U.-L., 2015, *Phys. Rev. D*, **91**, 083514
- Smirnov O. M., 2011, *A&A*, **527**, A106
- Smirnov O. M., Tasse C., 2015, *Monthly Notices of the Royal Astronomical Society*, **449**, 2668
- Tegmark M., Zaldarriaga M., 2009, *Phys. Rev. D*, **79**, 083530
- Tingay S. J., et al., 2013, *Publ. Astron. Soc. Australia*, **30**, e007
- Torchinsky S. A., Olofsson A. O. H., Censier B., Karastergiou A., Serylak M., Picard P., Renaud P., Taffoureau C., 2016, *A&A*, **589**, A77
- Wang X., Tegmark M., Santos M. G., Knox L., 2006, *ApJ*, **650**, 529
- Wolz L., Abdalla F. B., Blake C., Shaw J. R., Chapman E., Rawlings S., 2014, *MNRAS*, **441**, 3271
- Wuensche C. A., the BINGO Collaboration 2018, *arXiv e-prints*, p. [arXiv:1803.01644](#)
- Wyithe J. S. B., Loeb A., Geil P. M., 2008, *MNRAS*, **383**, 1195
- Zarka P., et al., 2015, in *2015 International Conference on Antenna Theory and Techniques (ICATT)*. 2015 International Conference on Antenna Theory and Techniques (ICATT). Kharkiv, Ukraine, [doi:10.1109/ICATT.2015.7136773](#), [https://hal.archives-ouvertes.fr/hal-01196457](#)
- Zhang J., Zuo S.-F., Ansari R., Chen X., Li Y.-C., Wu F.-Q., Campagne J.-E., Magneville C., 2016a, *Research in Astronomy and Astrophysics*, **16**, 158
- Zhang J., Ansari R., Chen X., Campagne J.-E., Magneville C., Wu F., 2016b, *MNRAS*, **461**, 1950
- van Haarlem M. P., et al., 2013, *A&A*, **556**, A2
- van Weeren R. J., et al., 2016, *ApJS*, **223**, 2

This paper has been typeset from a \LaTeX file prepared by the author.